Research Article | Vol. 32, No. 13 / 17 Jun 2024 / Optics Express 22781
Optics EXPRESS

In-water lidar simulations: the ALADIN ADM-Aeolus backscattered signal at 355 nm

DAVIDE D'ALIMONTE,[1,*] GIAN LUIGI LIBERTI,[2] MARCO DI PAOLANTONIO,[2,3] TAMITO KAJIYAMA,[1] NOEMI FRANCO,[3] PAOLO DI GIROLAMO,[3] AND DAVIDE DIONISI[2]

[1]AEQUORA, Lisboa, Portugal
[2]Institute of Marine Sciences (ISMAR), Italian National Research Council (CNR), Rome, Tor Vergata, Italy
[3]Scuola di Ingegneria, Università degli Studi della Basilicata, Potenza, Italy
*davide.dalimonte@aequora.org

Abstract: The Lidar Ocean Color (LiOC) Monte Carlo code has been developed to simulate the in-water propagation of the lidar beam emitted by the ALADIN ADM-Aeolus instrument in the ultraviolet (UV) spectral region (~ 355 nm). To this end, LiOC accounts for reflection/transmission processes at the sea surface, absorption and multiple scattering in the water volume, and reflection from the sea bottom. The water volume components included in the model are pure seawater, Chlorophyll-*a* concentration (Chl-*a*), Colored Dissolved Organic Matter (CDOM), and/or a generic absorbing species. By considering the transmission/reception measurement geometry of ALADIN ADM-Aeolus, the study documents the variability of the normalized backscattered signal in different bio-optical conditions. The potential for data product retrieval based on information at 355 nm is considered by developing a demonstrative lookup table to estimate the absorption budget exceeding that explained by Chl-*a*. Results acknowledge the interest of space programs in exploiting UV bands for ocean color remote sensing, as, for instance, addressed by the PACE mission of NASA.

1. Introduction and background

In the last decades, Ocean Color (OC) space programs have delivered time-series and global distributions of seawater constituents for environmental investigations and climate studies, such as Chlorophyll-*a* concentration (Chl-*a*), absorption of Colored Dissolved Organic Matter (CDOM), and Total Suspended Matter (TSM). Since passive remote sensing with sunlight as a radiation source cannot retrieve depth-resolved quantities, these products, computed with bio-optical algorithms using water reflectance as input, are averaged values in the surface water layer. Additional information on the biochemical structure of seawater constituents as a function of depth would be relevant for estimating primary production and analyzing the Oceanic Mixed Layer.

The possibility of retrieving the vertical distribution of seawater constituents from the water reflectance spectrum has been investigated with a Neural Network (NN) trained with in-situ measurement profiles [1]. The validity of NN results is, however, only ensured in water types equivalent to those of the training dataset [2,3]. Unlike standard OC products, lidar systems allow, in principle, the direct retrieval of profiles of seawater optical constituents. Evaluating the lidar technology to determine seawater optical properties as a complement to passive remote sensing is of growing interest to space agencies, and it is the motivation behind the present work.

The lidar viewing geometry, the system emission and acquisition characteristics, and the signal-to-noise ratio (SNR) are core aspects to address OC remote sensing applications and the accuracy of related data products. To this end, lidar OC results were investigated with shipborne/airborne [4] and orbiting systems designed for atmospheric applications [5–12]. The

#510919 https://doi.org/10.1364/OE.510919
Journal © 2024 Received 15 Nov 2023; revised 15 Jan 2024; accepted 26 Jan 2024; published 6 Jun 2024

Optics EXPRESS

present study progresses this research line by considering as a specific case study the Atmospheric Laser Doppler Instrument (ALADIN) launched in 2018 onboard the Aeolus orbiting platform within ESA's Atmospheric Dynamics Mission (ADM) and recently decommissioned (March 2023) [13].

ALADIN features unique characteristics as a case study for OC data retrieval since it is the first spaceborne system based on the emission of the 3rd Nd-YAG harmonic ($\approx$ 355 nm) with additional High Spectral Resolution Lidar (HSRL) capabilities. The HSRL relevance in determining seawater optical properties has been analyzed in various studies [14–16]. Nevertheless, after the pioneering mission LIdar Technology Experiment (LITE) launched onboard the Discovery Space Shuttle in September 1994, ALADIN has been the sole spaceborne lidar operating in the ultraviolet (UV). In this spectral domain, Chl-*a* is not the dominant absorption component, which allows retrieving other properties of interest, such as CDOM absorption [17]. Precisely, the water leaving reflectances in the ~350 to 400 nm interval can provide relevant information (and currently operationally not implemented) to accurately separate phytoplankton pigment absorption from CDOM absorption and to verify the CDOM absorption spectral slope, which can then be related to its terrestrial and aquatic sources [18,19].

Exploiting the UV range for OC purposes is of specific interest to the Plankton, Aerosol, Cloud, Ocean Ecosystem (PACE) program of NASA [20,21]. Studies investigating OC product retrieval of currently available instruments covering the UV region but not designed explicitly for OC applications have also been performed. For instance, Oelker et al. [22] exploited the UV and visible wavelengths of the TROPOMI sensor onboard Sentinel-5P to infer the in-water diffuse attenuation coefficient. Exploring ALADIN capabilities for applications other than its primary wind retrieval was also prioritized by the CDOM-Proxy Retrieval From Aeolus Observations (COLOR) project of the European Space Agency. This project aims to understand the potential to determine ocean optical properties at 355 nm by analyzing the ocean sub-surface backscattered component of the signal acquired by ALADIN. Within this framework, the present study focuses on identifying conditions where the sea surface, the water volume, and the sea bottom can affect the acquired signal and, on this basis, verify the dynamics of ALADIN measurements in different bio-optical regimes. A companion paper will present results about the corrections for the atmospheric contribution and the actual data product retrieval from lidar spaceborne measurements [23]. The present study focuses instead on detailing the Lidar Ocean Color (LiOC) Monte Carlo (MC) simulator developed to model lidar propagation in the water column.

LiOC solves the radiative transfer using general-purpose ray-tracing functions for ocean optics investigations [24–27]. Various Radiative Transfer Models (RTMs) have considered the lidar beam propagation in the atmosphere and the ocean [17,28,29,29–36]. The new code has been implemented to overcome any limitation of other simulation schemes by fully accounting for ALADIN observation geometry and using bio-optical algorithms to accurately model seawater optical properties at the 355 nm measurement wavelength. The validity and applicability of the simulation code developed in this work are also of interest to other missions with a higher oceanic focus, and in particular to the bilateral ASI-NASA space lidar mission CALIGOLA (Cloud and Aerosol Lidar for Global-Scale Observations of the Ocean-Land-Atmosphere System), which recently entered phase B1 [37,38]. Relevant CALIGOLA characteristics are a planned higher ocean penetration and the laser emission at 355 and 532 nm.

The work organization is as follows. Section 2 describes the simulation framework. ALADIN simulation results are presented and discussed in Section 3. In particular, a lookup table (LUT) is addressed in Section 3.4 as a demonstrative study case for retrieving seawater optical properties from ALADIN measurements. LiOC results are also compared to an analytical model in Section 3.5 for a consistency analysis. The summary of findings and remarks of Section 4 completes the work.

Optics EXPRESS

2. Data and methods

This section describes the developed RTM. Radiometric quantities to simulate the lidar backscattered signal are introduced in Sec. 2.1. Sections 2.2 to 2.4 present the modeling of radiative processes and optical properties at the sea surface, seawater volume, and sea bottom. Details on the implementations of the MC simulation code are reported in Sec. 2.5. Finally, the specific measurement and viewing geometry settings needed to simulate ALADIN observations of the water volume are detailed in Sec. 2.6. It is noted that the analysis of the contribution of the atmosphere to the backscattered signal, and demonstrations based on actual ALADIN measurements are out of the study scope.

2.1. Quantities for analyzing the lidar beam in seawater

Given a P amount of photons incident at the sea surface, the RTM simulates the number of photons backscattered (P^T) towards the receiving system. Note that the explicit dependence from wavelength is not reported unless necessary. This quantity includes the contributions from the sea surface (P^s), the sensed water volume (P^w), and the sea bottom (P^b):

$$P^T = P^s + P^w + P^b. \tag{1}$$

Depending on environmental and measurement conditions, some contributions to the total retrieved signal might become negligible, and understanding the relevance of the different terms in the case of ALADIN measurements is a core part of the present work.

In order to compare the simulation results with measurements, whose absolute value depends on the instantaneous laser emission power, the ratio of the above quantities and the sea surface incident photons P (*i.e.*, $P^x_{\mathrm{n}} = P^{\mathrm{x}}/P$, where $x = T,\ s,\ w,\ b$) is used in the rest of the study.

2.2. Sea-surface radiative properties

The developed model accounts for the interaction of the radiation with the atmosphere/ocean interface (*i.e.*, the sea surface), which is assumed to be a non-absorbing layer. Consequently, radiatively speaking, it is sufficient modeling the reflectance to know the transmittance. Sea surface reflectance depends on seawater's refraction index and surface waves. The Cox and Munk slope distribution is adopted for modeling wind-driven roughness [39]. Let x-y-z denote a Cartesian system with x-y in a horizontal plane. The slope at a point of the wind-roughed sea surface with an inclination angle θ_x along the x-axis is defined as $\zeta_x = \tan(\theta_x) = {}^{\Delta_z}/_{\Delta_x}$, and the Probability Density Function (PDF) of the wave slope $p(\zeta_x)$ is expressed as:

$$p(\zeta_x) = \frac{1}{\sqrt{2\pi\sigma^2_{\zeta_x}(v_w)}} e^{-\frac{\zeta_x^2}{2\sigma^2_{\zeta_x}(v_w)}}, \tag{2}$$

where $\sigma_{\zeta_x}(v_{\mathrm{w}})$ is the standard deviation of ζ_x as a function of the wind intensity speed v_w [m s^{-1}]. Analogous definitions apply for the PDF of the wave slope $p(\zeta_y)$ along the y-axis.

The following simplifying assumptions are made as in Mobley et al. [40,41]: 1) the slope variance does not depend on wind direction, and 2) the sea surface is still in the absence of wind. The resulting parameterization of the slope variance is then:

$$\sigma^2_{\zeta_x}(v_w) = \sigma^2_{\zeta_y}(v_w) = \sigma^2_{\zeta}(v_w) = 0.00254 \cdot v_w. \tag{3}$$

The probability that, the slope θ and the orientation ϕ at the sea surface are within the respective $\Delta\theta$ and $\Delta\phi$ ranges that allow for back-reflection is denoted as $P(\theta \in \Delta\theta,\ \phi \in \Delta\phi)$. Based on

Optics EXPRESS

the ergodic-cap model [42], the probability that the geometrical back-reflection conditions are satisfied is

$$P(\theta \in \Delta\theta,\ \phi \in \Delta\phi) = \frac{\Delta\phi}{2\pi}\left[-\exp\left(-\frac{\tan^2\left(\theta_g + \frac{\Delta\theta}{2}\right)}{2\sigma_\zeta^2(v_w)}\right) + \exp\left(-\frac{\tan^2\left(\theta_g - \frac{\Delta\theta}{2}\right)}{2\sigma_\zeta^2(v_w)}\right)\right] \cdot \frac{1}{\cos(\theta_g)} \quad (4)$$

where θ_g is the observation zenith angle. The back-reflected photon fraction is then computed as

$$P_n^s(v_w) = P(\theta \in \Delta\theta,\ \phi \in \Delta\phi) \cdot R_F, \quad (5)$$

with R_F denoting the Fresnel unpolarized spectral back-reflection. The reflected photon fraction can be finally expressed as a function of the solid angle of observation Ω_r^a assuming for simplicity $\Delta\theta \cong \Delta\phi$ and determining the angle increment by solving $\sin\theta\Delta\theta\Delta\phi = \Omega_r^a$ as $\Delta\theta = \Delta\phi = \sqrt{\Omega_r^a/\sin\theta}$.

The foam presence starts when the wind speed rises above 5–10 m/s [43–45], and a threshold value of 8 m/s is assumed here. It is anticipated that this limit corresponds to conditions where the signal back-reflected by the sea surface reflectance starts contributing to the detected signal (see Sec. 3.1). Moreover, accounting for sea foam contribution needs the knowledge of its spectral properties [46] that are poorly documented in this spectral range. For this reason, observations in high wind conditions are flagged when developing the algorithm for retrieving seawater optical properties [23], which justifies the omission of sea foam contribution in the presented model.

2.3. Seawater optical properties

2.3.1. Inherent optical properties

Seawater Inherent Optical Properties (IOPs) are expressed in terms of 1) absorption coefficient a [m^{-1}], 2) attenuation coefficient c [m^{-1}] or scattering coefficient b [m^{-1}] depending on the modeled seawater component and reference publications, and 3) scattering Phase Function (PF) $\tilde{\beta}$ [sr^{-1}]. In addition to the pure seawater, the IOPs account for the contribution of 1) Chl-a [mg m^{-3}] in typical Case-1 waters and 2) independent CDOM sources of varying relevance. The present study assumes that the contribution of suspended particles that do not covary with Chl-a is negligible and verifies the feasibility of using ALADIN data for retrieving the CDOM absorption fraction that Chl-a cannot explain [20,22].

The rationale for this hypothesis is to verify the variability of the 355 nm lidar pulse backscattered by the ocean P_n and its potential application for CDOM retrieval. Moreover, within the frame of Aeolus observation inversion, backscattering of particulate matter is assumed to be negligible compared to backscattering from pure seawater. Accounting for additional optical properties of particulate matter would be relatively straightforward once the IOPs of the mixture are accounted for in the RTM and additional input information is available (*i.e.*, P_n at different wavelengths).

Specific IOP parameterizations are detailed as follows. The total absorption coefficient $a_{tot}(\lambda)$ is defined as

$$a_{tot}(\lambda) = a_w(\lambda) + a_p(\lambda) + a_\mathrm{CDOM}(\lambda), \quad (6)$$

where λ [nm] is the wavelength, w indicates the contribution of pure seawater, p accounts for both pigmented and non-pigmented particulate matter.

The pure seawater absorption $a_w(\lambda)$, for selected temperature (T = 16 °C) and salinity (S = 35.5 PSU), is derived from WOPP data [47] applying the coefficient computed by Mason et al. [48]. The value of seawater absorption at 355 nm is $a_w(355) = 0.00097\ \mathrm{m}^{-1}$.

Optics EXPRESS

The absorption due to the pigmented and not-pigmented particulate matter $a_p(\lambda)$ as a function of Chl-a, is

$$a_p(\lambda) = A(\lambda) \cdot \text{Chl-}a^{E(\lambda)}, \tag{7}$$

where the coefficients $A(\lambda)$ and $E(\lambda)$ are the "mid-range UV parameters" [40, see also related studies therein]. Specific values at 355 nm are $A(355) = 0.040\,\text{m}^{-1}$ and $E(355) = 0.766$.

The assumed CDOM absorption spectral dependence is

$$a_{\text{CDOM}}(\lambda) = a_{\text{CDOM}}(\lambda_0) \cdot \exp[-S(\lambda - \lambda_0)], \tag{8}$$

with $S = 0.014\ \text{nm}^{-1}$ [49].

A generalized version of the total absorption budget is adopted in the present work:

$$a_{tot}(\lambda) = [a_w(\lambda) + a_p(\lambda)] + \Delta a, \tag{9}$$

where Δa varies to cover the variability of seawater absorption independently from Chl-a. This scheme permits the creation of LUT for the ALADIN measurements inversion (see Sec. 3.4) without an a priori choice of $a_{\text{CDOM}}(\lambda)$, leaving its selection to the post-processing stage once the Δa value has been retrieved from the lidar measurements. The rationale is that the relationship between a_{CDOM} and a_p (which, in its turn, depends on Chl-a) can vary in different environmental regimes [40,50,51]. The algorithm considered as a reference in this study to relate absorption contribution due to CDOM to the absorption of suspended particles in Case-1 waters is that proposed by Pitarch [50]

$$a_{\text{CDOM}}(\lambda) = 0.6154 \cdot a_p(440) \cdot \exp[-0.014(\lambda - 440)]. \tag{10}$$

The total seawater attenuation $c(\lambda)$ is

$$c_{tot}(\lambda) = c_w(\lambda) + c_p(\lambda). \tag{11}$$

The pure seawater contribution $c_w(\lambda)$ is determined by adding the scattering $b_w(\lambda)$ and the absorption $a_w(\lambda)$ coefficients

$$c_w(\lambda) = a_w(\lambda) + b_w(\lambda). \tag{12}$$

The seawater scattering at 355 nm is $b_w(355) = 0.011\,\text{m}^{-1}$ [47], and hence, the attenuation coefficient is $c_w(355) = 0.012\,\text{m}^{-1}$. The attenuation coefficient of the particulate matter $c_p(\lambda)$ is expressed as

$$c_p(\lambda) = c_o \cdot [\text{Chl-}a]^m \cdot \left(\frac{\lambda}{660}\right)^{\nu}, \tag{13}$$

with $c_o = 0.407$, $m = 0.706$ [52] and, based on results presented by Morel [53],

$$\nu = \begin{cases} 0.5 \cdot [\log_{10}(\text{Chl-}a) - 0.3] & \text{for } 0.02 < \text{Chl-}a < 2 \\ 0 & \text{for Chl-}a \geq 2 \end{cases} \tag{14}$$

The spectral absorption and attenuation coefficients are presented in Fig. 1. The position of ALADIN 355 nm emission wavelength is highlighted for reference, together with the second Nd-YAG harmonic (*i.e.*, 532 nm).

Although the present work only considers the 355 nm emission wavelength, Fig. 1 also highlights IOPs values at 532 nm (which was exploited by previous satellite lidar applications and will also be further considered in the forthcoming CALIGOLA mission) to document the contribution of different IOPs in the UV and visible spectral regions. Comparing spectral properties at these bands shows that the reduced contribution of pure seawater favors the sensitivity to other components, particularly the significance of CDOM absorption with respect to Chl-a.

Optics EXPRESS

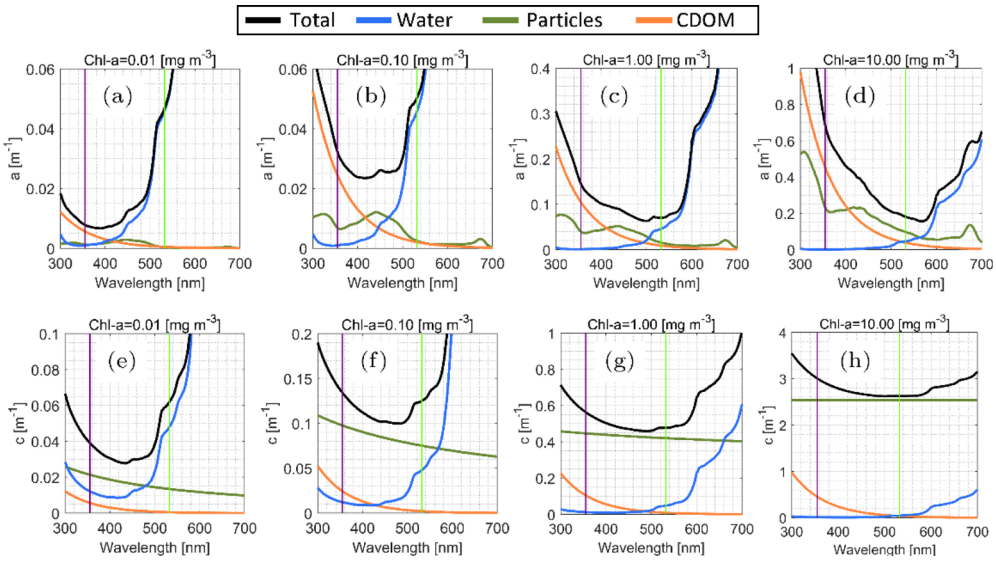

Fig. 1. Absorption and attenuation spectra are presented for Chl-$a = 0.01, 0.1, 1, 10$ mg m^{-3} in row panels from left to right. The top and bottom rows report absorption and attenuation spectra, respectively. The position of the ALADIN emission wavelength at 355 nm and that of the second harmonic at 532 nm are highlighted for reference.

The scattering coefficient b is the integral over the solid angle of the Volume Scattering Function (VSF), indicated with the symbol β and with units of [m^{-1} sr^{-1}]

$$b = \int_{4\pi} \beta(\Omega) d\Omega = \int_0^{2\pi} \int_0^{\pi} \beta(\Psi, \Phi) \sin(\Psi) d\Psi d\Phi, \tag{15}$$

where Ψ and Φ are the zenith and azimuth scattering angles, respectively, in the ray propagation reference system (Fig. 2). Assuming the azimuth symmetry of the VSF, Eq. (15) can be reviewed as

$$b = 2\pi \int_0^{\pi} \beta(\Psi) \sin(\Psi) d\Psi. \tag{16}$$

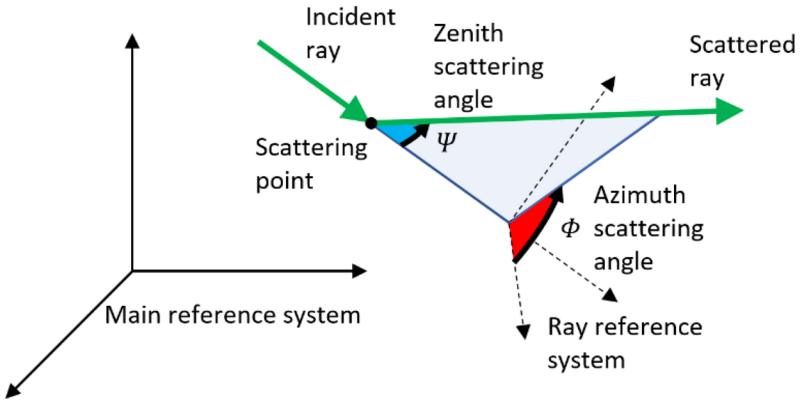

Fig. 2. Schematic of the zenith Ψ and azimuth Φ scattering angles.

Optics EXPRESS

The scattering phase function (PF) is the ratio between the VSF and b

$$\tilde{\beta}(\Psi) = \frac{\beta(\Psi)}{b} \tag{17}$$

hence the integral of $\tilde{\beta}(\Psi)$ over the solid angle is equal to 1. The scattering phase function accounts for the contribution of particles $\tilde{\beta}_p$ and pure seawater $\tilde{\beta}_w$ as

$$\tilde{\beta}(\Psi) = \frac{b_p}{(b_p + b_w)} \cdot \tilde{\beta}_p(\Psi) + \frac{b_w}{(b_p + b_w)} \cdot \tilde{\beta}_w(\Psi). \tag{18}$$

PF models of particle scattering presented in the literature include those published by Fournier and Forand [54,55] and Morel et al. [53]. The present study relies on Morel's formulation (Fig. 3(a)), which determines $\tilde{\beta}_p$ as

$$\tilde{\beta}_p(\Psi, \text{Chl-}a) = \alpha_s(\text{Chl-}a)\, \tilde{\beta}_s(\Psi) + \alpha_l(\text{Chl-}a)\, \tilde{\beta}_l(\Psi) \tag{19}$$

where the PFs of small and large particles — $\tilde{\beta}_s(\theta)$ and $\tilde{\beta}_l(\theta)$, respectively — are computed with the T-Matrix scheme [56,57]. The weighting coefficients α_s and α_l are:

$$\alpha_s(\text{Chl-}a) = 0.855 \cdot [0.5 - 0.25\log_{10}(\text{Chl-}a)] \quad \text{and} \quad \alpha_l(\text{Chl-}a) = 1 - \alpha_s(\text{Chl-}a). \tag{20}$$

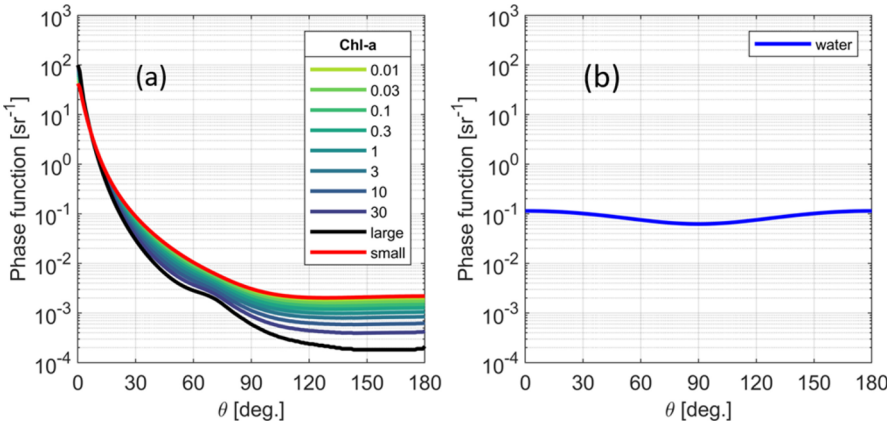

Fig. 3. Scattering phase functions computed with the method presented by Morel et al. [53] are presented in Panel (a). The scattering phase function of pure seawater is shown in Panel (b).

The phase function of pure seawater $\tilde{\beta}_w$ is shown in Fig. 3(b).

2.3.2. Diffuse attenuation coefficient and the lidar effective attenuation coefficient

Apparent optical properties (AOPs) depend on the illumination, observation geometry, and IOPs. The AOP of interest to this analysis is the diffuse attenuation coefficient K_d of downward irradiance E_d, defined as

$$K_d(z)E_d(z) = -\frac{dE_d(z)}{dz}. \tag{21}$$

The K_d value can be derived from 1) in-situ measurements of E_d as a function of depth, 2) bio-optical algorithms based on remote sensing data [58], and 3) IOPs, taking into account the

Optics EXPRESS

illumination geometry [59]. The K_d expression in this latter case is

$$K_d(z) = \frac{a(z) + b_b(z)}{\mu}, \tag{22}$$

where $a(z)$ and $b_b(z)$ are the absorption and backscattering coefficients, respectively, and $\mu = \cos(\theta_r^w)$ with θ_r^w representing the in-water angle of the incident beam. This beam originates from the sun in case of passive ocean color radiometry or is the emitted laser beam in case of lidar application.

The definition of the lidar effective attenuation coefficient K_{lid} is formally equivalent to that of the diffuse attenuation coefficient

$$K_{\text{lid}}(r)P(r) = -\frac{dP(r)}{dr}, \tag{23}$$

where P is the lidar radiant power and $r = z/\mu$ as a function of depth. Gordon [60] has shown how the K_{lid} value can vary between the diffuse attenuation coefficient K_d defined as a quasi-inherent optical property (*i.e.*, defined in the conditions of no atmosphere and with the sun at the zenith) and the beam attenuation coefficient c. Specific cases of study related to ALADIN measurements are in the results section.

2.4. Sea-bottom reflectance properties

The study assumes a Lambertian sea bottom with a Bidirectional Reflectance Distribution Function BRDF_b for incident direction (θ_i, ϕ_i) and reflection direction (θ_r, ϕ_r) defined as

$$\text{BRDF}_\text{b}(\theta_i, \phi_i \rightarrow \theta_r, \phi_r) = \frac{\rho_\text{b}}{\pi}, \tag{24}$$

where ρ_b is the reflectivity. The ρ_b value of the Lambertian surface is equal to that of the irradiance reflectance $R_\text{b} = {}^{E_\text{u}}/_{E_\text{d}}$, where E_u and E_d are the upward and downward irradiance values.

The probability density function $p_\text{b}(\theta, \phi)$ that the bottom reflects a photon in the (θ, ϕ) direction is

$$p_\text{b}(\theta, \phi) = \rho_\text{b}\frac{1}{\pi}\cos(\theta). \tag{25}$$

Highly reflective coral sand with $\rho_b = 0.2$ [40,61,62] is later considered to identify the depth limit where the sea bottom can affect ALADIN measurements. The depth range where the bottom, if included in the geometry of the lidar bin, does not influence the backscattered signal is discussed in the results section.

2.5. Monte Carlo ray tracing

The LiOC simulations are executed in a water column with lateral dimensions L_x and L_y, and depth Z_{max}. In the present study L_x = 400 m, L_y = 400 m, and Z_{max} = 500 m (reduced depth values are considered to evaluate the bottom contribution). The sea surface at the upper boundary can be flat or account for surface waves as a function of wind speed [27,39,63]. Seawater optical properties are horizontally homogeneous and can vary vertically in layers of arbitrary depths. Results presented in this study refer to a still sea surface and no stratifications in the water column. The lower boundary is a Lambertian surface (Sec. 2.4). The number of traced photons is defined on a case-by-case basis to ensure the reproducibility of results.

The ray starting point and incoming direction (θ_g) are defined in agreement with the footprint, the orientation, and the solid angle of the ALADIN laser beam (Sec. 2.3). The ray's initial weight m is 1 (denoting the weight as m for mass instead of using the w symbol because this latter already represents *in-water* quantities). The Snell and Fresnel equations define the refraction

Optics EXPRESS

direction and the weight scaling (surface transmittance T_s) as the incident ray crosses the air-water interface. In the water bin, the ray-tracing path l is computed as

$$l = -\frac{\log(u)}{c}, \tag{26}$$

where $u \in \mathcal{U}(0,1)$ — *i.e.*, uniform distribution between 0 and 1 — and c is the attenuation coefficient.

Upon scattering at the end of each tracing path (*i.e.*, dots labeled as B, C, D, and E in Fig. 4), the new ray direction is sampled from the phase function $\tilde{\beta}(\Psi)$. The zenith scattering angle Ψ is derived from the cumulative distribution function (CDF) of $\tilde{\beta}(\Psi)$ by generating a random number $u \in \mathcal{U}(0,1)$ and solving $\mathrm{CDF}(\Psi) = u$ for Ψ. The azimuth scattering angle Φ follows instead a uniform distribution $\mathcal{U}(0, 2\pi)$. The scattered rays correspond to the BC, CD, and EF solid lines in Fig. 4. Following Gordon [60], the weight of the scattered ray and the contribution to the backscattered signal is determined depending on which of the two conditions described next is satisfied.

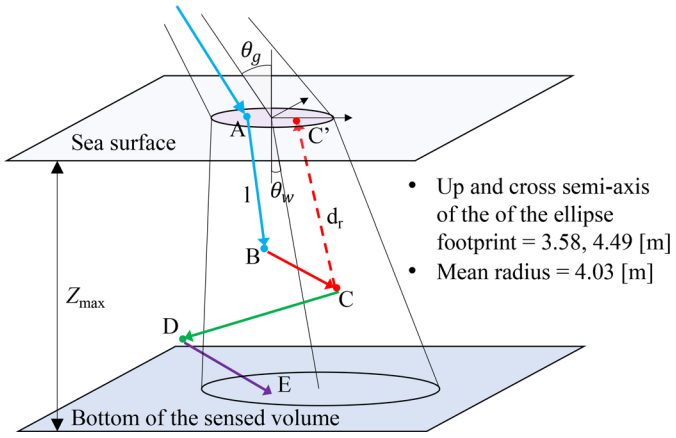

Fig. 4. Ray tracing scheme.

Condition 1 occurs when it is possible to identify a trajectory inside the in-water acceptance solid angle $\Delta\Omega_w^A$ (*e.g.*, dashed CC' line) from the scattering point to the to the surface. The scattering probability in a direction towards the receiver $R(\Psi_r)$ is computed as

$$R(\Psi_r) = \tilde{\beta}(\Psi_r)\Delta\Omega_w^A. \tag{27}$$

The path weight-reduction factor $Q(d_r)$ is additionally determined as

$$Q(d_r) = \mathrm{e}^{-c \cdot d_r} \tag{28}$$

where d_r is the distance between the scattering point and the sea surface exiting point. The total weight reduction $C(\Psi_r, d_r)$ is finally calculated as

$$C(\Psi_r, d_r) = R(\Psi_r)Q(d_r)T_s, \tag{29}$$

where T_s is the Fresnel transmission for the outcoming angle (θ_w) across the sea surface (incoming and outcoming T_s are assumed the same). The s_i contribution to the retrieved signal is hence

$$s_i = m_i \cdot \omega_0 \cdot C(\Psi_r, d_r), \tag{30}$$

Optics EXPRESS

where i is the scattering order (*i.e.*, $i = 1$ for single scattering and $i = 2, 3, \ldots$ for multiple scattering) and ω_0 is the single scattering albedo

$$\omega_0 = b/c \tag{31}$$

expressing the probability that the ray is not absorbed when interacting with a seawater molecule or a suspended particle. The value of P_n^w is the sum of s_i values of all rays and any scattering order, divided by the number of emitted photons N. The weight m_{i+1} of the ray scattered according to the phase function (CD path) is obtained as the difference between the initial weight before the scattering m_i and the computed signal s_i

$$m_{i+1} = m_i - s_{i.} \tag{32}$$

To study the K_{lid} profile, the depth of the scattering event is defined as half the sum of the ray-tracing path lengths. The vertical profile of the contribution to the backscattered signal is computed by binning the scattering depth with a 10 cm increment. Finally, the ray stops contributing to the backscattered signal P_{n} when its cumulative path length L overcomes a threshold L_{max}. An accurate L_{max} definition is not a critical aspect of the present study because 1) the pulse duration of 30 ns does not allow for resolving vertical details of in-water optical properties (see Sec. 2.6), and 2) P_{n} reduces rapidly as the cumulative path length increases (see Sec. 3.2). The current simulation setting is then aimed to ensure that the full backscattered pulse is collected. The capability to determine P_{n} as a function of L intervals is, however, a LiOC feature of interest to other lidar missions, such as Aeolus-2 and CALIGOLA, which will rely on 355 nm pulses with shorter durations. In addition, specific data acquisition approaches based on signal oversampling are under consideration for CALIGOLA to target vertical resolutions in the order of 1 m.

Condition 2 corresponds to the alternative case in which reaching the surface from the scattering point is impossible with a trajectory inside the in-water acceptance solid angle. In this case, there is no contribution to the backscattered signal (*e.g.*, point D of Fig. 4), and the ray weight is updated as

$$m_{i+1} = m_i \cdot \omega_0. \tag{33}$$

Hence, the standard rule to sample the new ray direction from the phase function applies.

2.6. ALADIN measurement setting and viewing geometry

ADM-Aeolus satellite operates in a polar, sun-synchronous orbit at an inclination of 97° with a mean altitude of 320 km [64]. The line-of-sight (LOS) of ALADIN is perpendicular to the satellite trajectory, pointing 35° from the nadir, corresponding to a satellite zenith angle at the surface of about 37° due to Earth curvature (Fig. 5). ALADIN [13] includes two receivers to measure the Doppler shift of the emitted laser wavelength (≈ 354.7 nm) due to the wind along the LOS: a double Fabry-Pérot spectrometer to measure Rayleigh scattering from air molecules (*i.e.*, Rayleigh channel) and a Fizeau spectrometer to measure Mie scattering from cloud droplets and aerosols (*i.e.,* Mie channel).

The laser emission frequency is 100 Hz, and the pulse duration is 30 ns. The vertical resolution can be set separately for the Mie and the Rayleigh channels with multiples of 250 m. In contrast, the height of the vertical layers depends on the altitude referenced to the World Geodetic System (WGS84) [65] ellipsoid.

For the numerical simulations, it is fundamental to reproduce the ALADIN viewing geometry correctly. Because of the slant viewing angle, the volume sensed by the instrument will be characterized by an elliptic geometry for the top and bottom surfaces of the volume. Neglecting the movement of the satellite, the geometry assumed in the model is the one relative to the Instantaneous Field of View (IFOV).

Optics EXPRESS

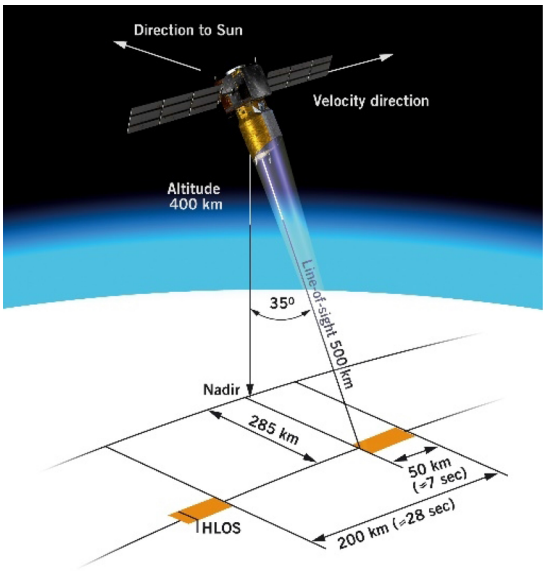

Fig. 5. Measurement geometry and coverage of ADM-Aeolus (Image: ESA – AOES Medialab).

The real component of the seawater refractive index defines the geometry of the sensed volume in the water. Figure. 6 shows the real part of the refractive index for different salinity and temperature values according to WOPP [47]. The variability over the expected range is less than 0.5%. In this study, the dependence of water refractive index on temperature and salinity is neglected, given the relatively low variability and the lack of reliable ancillary data for their estimation. The value of the refraction index is then set to $n = 1.356$. This value encompasses a set of likely scenarios shown in Fig. 6. The most significant impact of this assumption is in the presence of significant temperature stratification, but its effect is lessened by the exclusion of optical stratifications (see Sec. 2.5).

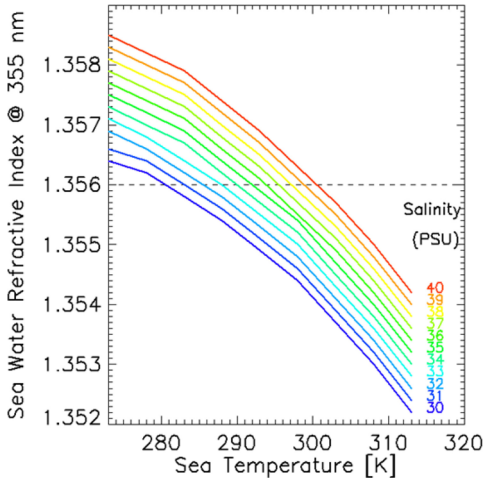

Fig. 6. Seawater real refractive index at 355 nm as a function of salinity and temperature according to WOPP [47]. The dashed horizontal line is the value assumed for this study.

Optics EXPRESS

In this study focused on modeling the ALADIN signal backscattered from the water volume, the variability of observation geometry, *e.g.,* orbit altitude and viewing angle, is neglected. The observation parameters for ALADIN simulations are reported in Table 1.

Table 1. ALADIN viewing geometry relevant variables.

Quantity	Symbol and value
Seawater real refractive index	$N = 1.356$
Viewing angle (ground)	$\theta_g = 37.041°$
Viewing angle (water)	$\theta_w = 26.4°$
Emitter solid angle (air)	$\Omega_a^E = 3.142\text{e-}10$ sr
Telescope solid angle (air)	$\Omega_a^T = 2.573\text{e-}10$ sr
Telescope solid angle (water)	$\Omega_N^T = 1.246\text{e-}10$ sr
Acceptance solid angle (water)	$\Delta\Omega_w^A = 5.470\text{e-}12$ sr

From a practical perspective, LiOC simulations aim to reproduce the water volume component of the so-called "ground-bin"; *i.e.*, the volume including the atmosphere-surface interface. In fact, due to the coarse vertical resolution of ALADIN measurements, the signal backscattered by the successive bin, which in principle consists entirely of water, is completely extinguished as shown by simulations (Sec. 3.2) and confirmed by the analyses of SNR of the observations [23]. Thus, based on the statistical analysis of the geometry of the ground bin observations, in this study we assume that the sensed depth (bottom depth of the ground-bin volume) is in the 70-200 m range.

3. Results

This section presents the contribution to the backscattering due to 1) the sea-surface reflection, 2) the water bin, and 3) the sea bottom. The implementation of a LUT to retrieve seawater optical properties from ALADIN measurements is then considered.

3.1. Sea-surface backscattering contribution

The ALADIN observation geometry was designed to minimize the sea-surface reflection effect. In this work, the contribution from a roughed surface reflectance (P_n^s) is determined as a function of the wind speed using the ergodic-cap method described in Sec. 2.2. Results are reported in Fig. 7. Although the analysis accounts for v_w in the range 2 to 16 m s^{-1}, the formation of white caps starts for wind speed values from about 8 m s^{-1} [66], which is a limit to the considered sea-surface backscattering model.

The received signal P_n^T can be used to determine optically active seawater constituents only if it is significantly larger than the contribution due to the back reflection by the sea surface P_n^s (otherwise, corrections should be applied). Assuming an average wind speed over the ocean of about $v_w = 6.6$ m s^{-1} [67], the corresponding reflected signal fraction is $P_n^s = 4 \cdot 10^{-18}$. If the real wind speed is not known and it is supposed that the ALADIN sea-bin measurement is acquired in mean wind-speed conditions, the signal fraction that is backscattered by the water column is then detectable if $P_n^T \gg 4 \cdot 10^{-18}$ (see Fig. 8). A lower threshold applies for reduced wind speed values.

3.2. Contribution of the in-water layer to the retrieved signal

The contribution of the in-water layer to the retrieved signal P_n^w could be derived directly from the lidar equation if K_{lid} were known. However, Gordon [57] has documented how K_{lid} varies as a function of both the lidar viewing geometry and the optical properties of the sensed water.

Optics EXPRESS

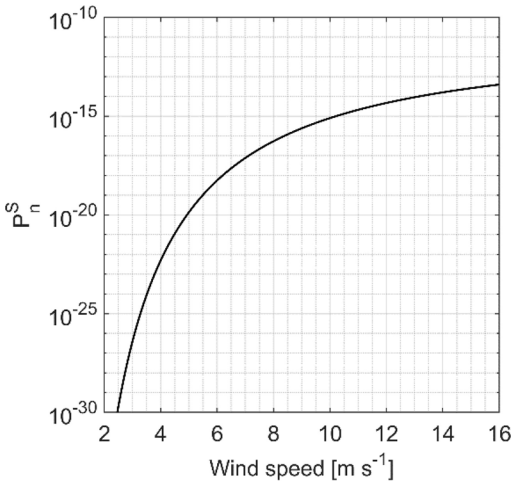

Fig. 7. Back-reflected radiant power as a function of the wind speed.

Precisely, the relationship between K_{lid} and the IOP depends on the parameter γ defined as the ratio between the radius of the footprint at the sea surface and the mean free path of photons in water given by 1/c. When γ is near zero, K_{lid} approaches the beam attenuation c [60], and single scattering events drive P_n^w. If the ratio γ is greater than 5, K_{lid} reaches values close to the diffuse attenuation coefficient for downwelling irradiance K_{d}, see Eq. (21), and in that case the multiple scattering contribution to P_n^w prevails. This reference scheme is considered in the present work. Alternatively, Phillips and Koerber [68] proposed that the upper and lower limits of K_{lid} are given by c and the water absorption coefficient a, respectively, depending on the receiver IFOV.

LiOC simulations account for the specific ALADIN viewing geometry. Since the footprint radius is about 4 m, a value of Chl-a equal to 0.01 mg m^{-3} corresponds to $\gamma = 0.16$ and hence to the single scattering regime. The Chl-a value of 10 mg m^{-3} leads instead to $\gamma = 12$ and, consequently, the dominance of multiple scattering. The contribution to P_n^w from different water depths and scattering orders, is analyzed with LiOC simulations shown in Fig. 8 (a), (b), and (c) for Chl-a equal to 0.01, 0.1, and 1 mg m^{-3}. The K_{lid} variation between values close to c and K_{d} at low and high Chl-a values, respectively, is highlighted, as well as the importance of single and multiple scattering contributions to P_n^w in the former and latter cases. Results indicate that, in the case of ALADIN measurements, K_{lid} cannot be univocally related to c or K_{d}, but varies between these two extremes depending on the marine optical conditions. In this scenario, numerical simulations are required to estimate K_{lid}, and analyze its dynamics. Note that the total signal distribution within the expected limiting values [60] supports the validity of these LiOC simulation results, as addressed more in detail in Sec. 3.5.

The percent contribution (cumulative distribution) to P_n^w due to a seawater layer from the surface down to the depth z is additionally presented in Fig. 9. Results indicate that P_n^w mostly originates from a limited upper water layer for Chl-a above 1 mg m^{-3}. In oligotrophic waters with Chl-a approaching 0.01 mg m^{-3}, the water layer that makes a significant contribution to P_n largely increases but a negligible fraction of the incident beam is returned from below 100 meters.

3.3. Fraction of back-transmitted radiant power due to reflection at the sea bottom

The backscattered radiant power ratio P_{n}^b due to the bottom reflection is considered in Fig. 10. The simulation accounts for Case-1 water conditions and still sea-surface ($v_w = 0$ m s^{-1}). The bottom contribution reduces as Chl-a increases. For instance, when Chl-a = 0.01 mg m^{-3} the

Optics EXPRESS

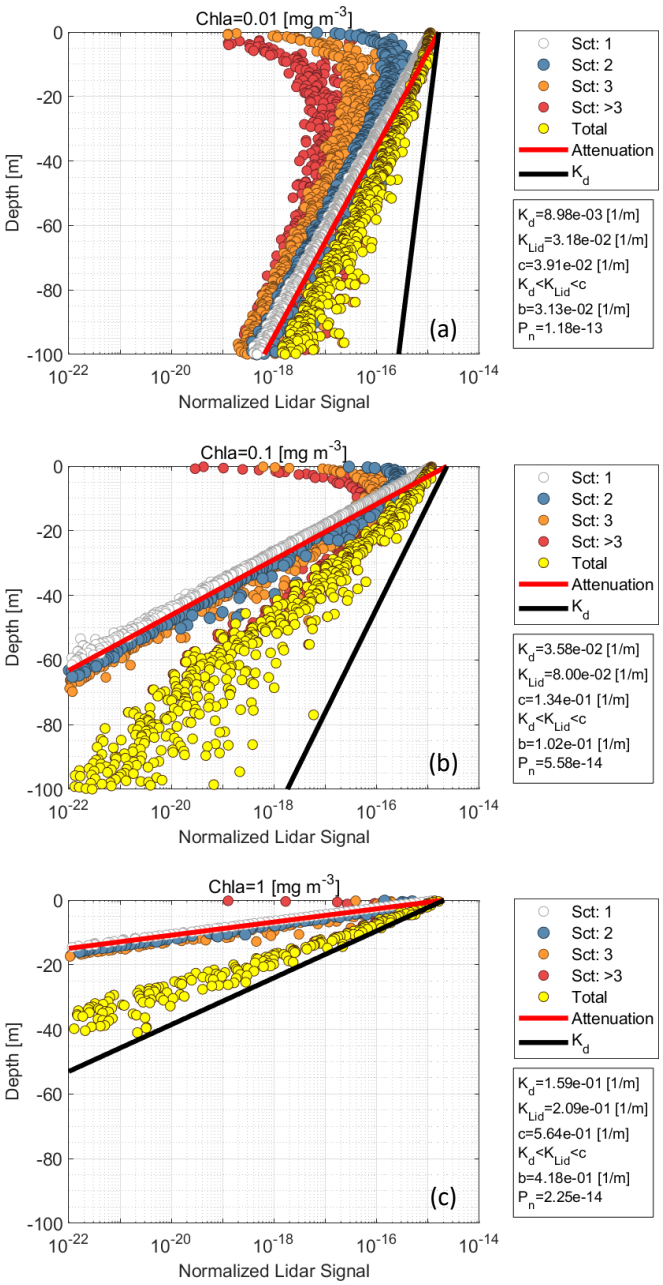

Fig. 8. Contribution of different water depths and scattering orders to the radiant power fraction P_n^w. Panels (a), (b) and (c) refer to Chl-*a* equal to 0.01, 0.1, and 1 mg m^{-3}, respectively.

Optics EXPRESS

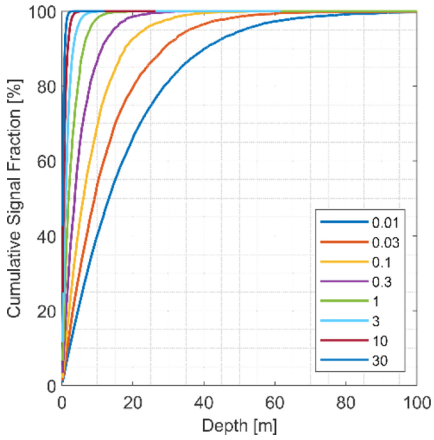

Fig. 9. Percent contribution to P_n^w as a function of depth for Chl-a in the range 0.01 to 30 mg m^{-3}.

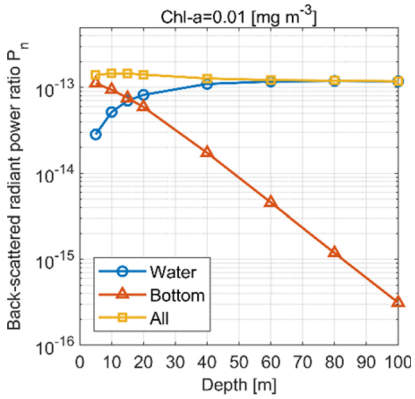

Fig. 10. Backscattered radiant power ratio P_n^b due to the bottom reflection (Chl - a = 0.01 mg m^{-3} and v_w = 0 m s^{-1}). The number of rays traced for each simulation case is $5 \cdot 10^5$.

bottom contribution to P_n^b becomes negligible if $z_b \geq 80$ m. As a conservative condition, in the present study, the bottom contribution shall be neglected when $z_b \geq z_{\max} = 100$ m.

3.4. *Look-up-table for the inversion of the ALADIN measurements in the sea bin*

When ALADIN measurements are limited to wind speed $v_w < 8$ m s^{-1} and sea bottom depth $z_b \geq 100$ m, simulation results indicate that $P_{\mathrm{n}}^w \gg P_{\mathrm{n}}^s$ and $P_{\mathrm{n}}^w \gg P_{\mathrm{n}}^b$, and hence in this case P_{n}^T is equivalent to P_{n}^w. These conditions represent the validity limit for the inversion of the ALADIN measurement into seawater optical properties discussed next.

MC simulation results are here applied to create, as a demonstrative case, a 3D LUT with Chl-a and P_n as input dimensions and a_{tot} as retrieved quantity (Eq. (9), see also Table 2). To construct this table, six Δa values are defined (*i.e.*, 0, 0.02, 0.1, 0.5, 2.5, 15.0 m^{-1}) to cover optically complex waters, including extreme cases. Chl-a values are varied from 0.001 to 100 mg m^{-3}. Extreme cases ensure data interpolation when reading the LUT. As an illustrative case, P_n^w values based on the parameterization proposed by Pitarch [50] for Case-1 waters are highlighted in gray in Table 2.

Optics EXPRESS

Table 2. LUT computed with LiOC to determine P_n^w as a function of IOPs. The total absorption values a_1 to a_6 correspond to the six Δa cases log-uniformly distributed in the 0 to 15 m^{-1} interval (see text for details). Note that the LUT coloring sequence is like that of Fig. 11.

Chl-*a*	Δa log-uniformly varied between 0 and 15 m^{-1}												Ref. case	
	P_n	a_1	P_n	a_2	P_n	a_3	P_n	a_4	P_n	a_5	P_n	a_6	P_n	a_{tot}
0.001	1.92E-13	0.0012	8.48E-14	0.0212	2.49E-14	0.1012	5.39E-15	0.5012	1.09E-15	2.5012	1.82E-16	15.0012	1.83E-13	0.0025
0.003	1.75E-13	0.0014	8.19E-14	0.0214	2.49E-14	0.1014	5.43E-15	0.5014	1.10E-15	2.5014	1.83E-16	15.0014	1.54E-13	0.0041
0.01	1.46E-13	0.0021	7.73E-14	0.0221	2.49E-14	0.1021	5.49E-15	0.5021	1.11E-15	2.5021	1.86E-16	15.0021	1.18E-13	0.0078
0.03	1.20E-13	0.0037	6.98E-14	0.0237	2.48E-14	0.1037	5.62E-15	0.5037	1.14E-15	2.5037	1.91E-16	15.0037	8.62E-14	0.015
0.1	9.10E-14	0.0078	6.17E-14	0.0278	2.47E-14	0.1078	5.87E-15	0.5078	1.19E-15	2.5078	2.00E-16	15.0078	5.61E-14	0.0322
0.3	6.84E-14	0.0168	5.16E-14	0.0368	2.40E-14	0.1168	6.10E-15	0.5168	1.27E-15	2.5168	2.14E-16	15.0168	3.60E-14	0.0658
1	4.82E-14	0.0408	3.98E-14	0.0608	2.21E-14	0.1408	6.71E-15	0.5408	1.42E-15	2.5408	2.41E-16	15.0408	2.23E-14	0.146
3	3.49E-14	0.0934	2.96E-14	0.1134	2.04E-14	0.1934	7.11E-15	0.5934	1.68E-15	2.5934	2.87E-16	15.0934	1.33E-14	0.3047
10	2.33E-14	0.2334	2.12E-14	0.2534	1.61E-14	0.3334	7.70E-15	0.7334	2.19E-15	2.7334	3.90E-16	15.2334	8.19E-15	0.6873
30	1.51E-14	0.5405	1.42E-14	0.5605	1.23E-14	0.6405	7.65E-15	1.0405	2.69E-15	3.0405	4.88E-16	15.5405	5.08E-15	1.4524
100	7.62E-15	1.3586	7.18E-15	1.3786	6.65E-15	1.4586	5.27E-15	1.8586	2.33E-15	3.8586	5.40E-16	16.3586	2.91E-15	3.3173

The LUT is shown in Fig. 11 as a function of a_{tot}, Chl-*a* and P_n^W. A fit is employed to interpolate unevenly spaced LUT data and highlight the continuous variation of a_{tot} over Chl-*a* and P_n^W. The LUT permits to retrieve $a_{tot}(355)$ from ALADIN ground-bin measurements under the following conditions. First, the ALADIN data are processed to exclude from the computation of P_n any contribution from the atmosphere not related to water, and to ensure that the measurements are not affected by the sea surface and sea bottom reflectance. Second, Chl-*a* concentration is obtained from an independent source (*e.g.*, Sentinel3/OLCI data products). Third, the contribution to the backscattered signal from suspended particles that do not covary with Chl-*a* is negligible. It is recalled that this latter assumption is implicit in all the analyses addressed in this work.

The a_{tot} value retrieved through the LUT can then be decomposed by removing the absorption due to Chl-*a* and pure seawater contributions to determine the Δa budget. The estimated Δa can be finally analyzed by considering different CDOM absorption models. It is remarked that this scheme avoids the necessity to create a specific LUT for each $a_{CDOM}(\lambda)$ algorithm [50,40,51]. A schematic of the data post-processing steps is presented in Fig. 12.

While recognizing the specificity of the considered case, it is remarked that the primary study objective is to present the MC simulation tool. In this context, the LUT-based approach represents a relevant example where the single-channel simulation results are used to estimate one marine optical property that mainly determines the variability of the backscattered signal (Fig. 1). It is also noted that well-characterized algorithms to retrieve Chl-*a* are available since a few decades. Instead, methods for an independent estimate of the CDOM (*i.e.*, not as Chl-*a* byproduct) still need consolidation. Hence, although with some limits, the study results meet the growing manifold interests of OC remote sensing to exploit information in the UV region, use spaceborne lidar observations, and understand better CDOM variability.

An additional relevant aspect is that, although Monte Carlo principles are spectrally equivalent, specific simulation results can vary significantly due to the dependence of IOPs on wavelength. In particular, by investigating the signal backscattered at 355 nm, the study acknowledged the growing OC interest in the UV region. The MC simulation tool was then designed to correctly

Optics EXPRESS

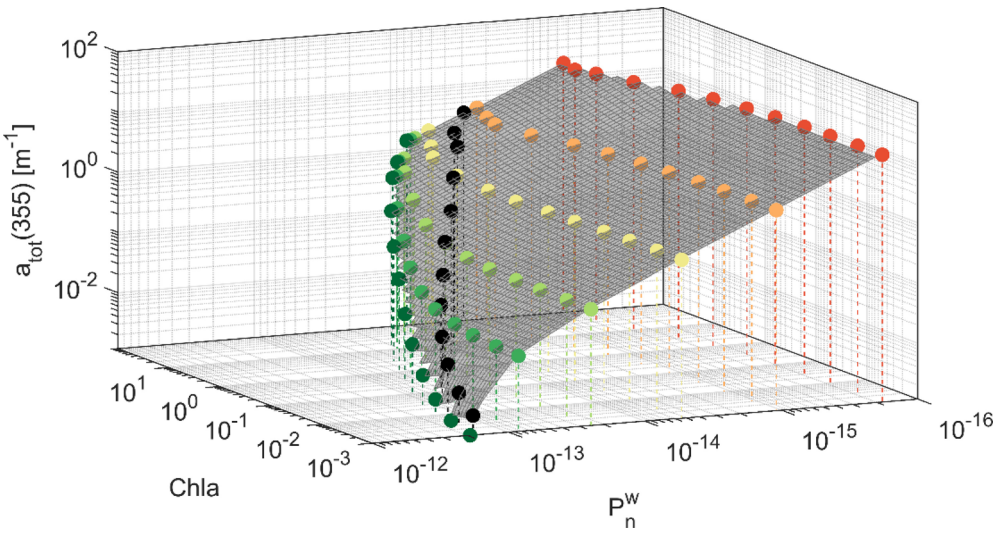

Fig. 11. LUT visualization. Filled circles correspond to the simulation runs of Table 2 (colors match, except for the black that corresponds to the data in the last table column shaded in gray).

$$b_{\mathrm{tot}}(355) = b_{\mathrm{w}}(355) + b_{\mathrm{p}}(355,\mathbf{Chl\text{-}}\boldsymbol{a})$$
$$\boldsymbol{a_{\mathrm{tot}}(355)} = \left[a_{\mathrm{w}}(355) + a_{\mathrm{p}}(355)\right] + \Delta a \quad \rightarrow \quad \mathrm{LiOC} \quad \rightarrow \quad \boldsymbol{P_n}$$

Fig. 12. Scheme to compute P_n: quantities in bold face correspond to LUT dimensions.

account for the geometry of the simulated lidar system (in the specific case, ALADIN ADM-Aeolus) regarding emitting/viewing angle and IFOV. Together with the spectrally dependent IOPs, such geometry characteristics are fundamental to correctly simulate the multiple scattering effect. In this respect, the LUT developed to retrieve the CDOM absorption represents a case study to demonstrate the possibility of relating the variability of the total absorption at 355 nm to the normalized backscattered signal acquired in a measurement geometry applied in a lidar reference mission.

3.5. *Consistency of simulation results*

The consistency of simulated results obtained with the developed radiative transfer tool has been tested with two approaches:

- by comparing with the same variable estimated from ALADIN measurements; and
- by comparing against the analytical expressions of the sub-surface signal, representing extreme cases, for which nominal, or typical equation values are used.

With both methods, an agreement in terms of order of magnitude and range was obtained. As mentioned in Sec. 1, the analysis of the ocean sub-surface backscattered component of the signal acquired by ALADIN is the objective of the COLOR project. In particular, the description of the data processing scheme to account for the atmospheric contribution goes beyond the scope of this work, and it will be detailed in a companion paper [23]. Here, the robustness of the presented simulation results is assessed based on a comparison against an estimate of the range

Optics EXPRESS

of variability obtained from the analytical expression of the measured signal. This approach allows independence from the applied parameters and focuses only on the consistency of Monte Carlo simulations.

The background-corrected signal $P^w(r_i)$ from elastic backscattering of a single laser pulse emission, returned to the receiver (*i.e.*, telescope) from the range r_i where $r = z/\cos(\theta_w)$—see Table 1—by a sensed water volume of (slant) thickness Δr is:

$$P^w(r_i) = P_0 M T_a^2 T_s^2 \Delta r \Delta\Omega_w^A \beta_\pi \exp[-2K_{\rm lid} r_i], \tag{34}$$

where P_0 is the emitted signal, M accounts for the overall instrument efficiency (or response), T_a is the total atmospheric transmittance, T_s is the sea-surface transmittance, $\Delta\Omega_w^A$ is the acceptance solid angle in water, and β_π is the VSF calculated at 180°. Note that the spectral and temporal dependencies are omitted in this equation and in the following ones.

To estimate the normalized signal P_n^w, we assume a scenario in agreement with LiOC simulation setting:

- unitary input signal $P_0 = 1$;
- no atmosphere $T_a = 1$;
- sea-surface transmittance $T_s = 0.974$;
- ideal instrument response $M = 1$;
- homogeneous water column within the sensed volume;
- lower bound of the sensed water volume $r_{\rm max} = 100$ m.

With these assumptions, Eq. (34) can be written as:

$$P_n^w(r_i) = T_s^2 \Delta r \Delta\Omega_w^A \beta_\pi \exp[-2K_{\rm lid} r_i] \tag{35}$$

Thus, the total normalized signal P_n^w for a number N of different water layers with the same optical properties and geometrical thickness Δr is:

$$P_n^w = \sum_{i=1}^{N} P_n^w(r_i) = T_s^2 \Delta r \Delta\Omega_w^A \beta_\pi \sum_{i=1}^{N} \exp[-2K_{\rm lid} r_i] \tag{36}$$

In the limit of $\Delta r \to 0$ the summation becomes an integral, allowing for computing P_N as:

$$P_n^w = \frac{T_s^2 \Delta\Omega_w^A \beta_\pi}{2K_{\rm lid}} \{1 - \exp[-2K_{\rm lid} r_{\rm max}]\} \tag{37}$$

For $r_{\rm max} = z_{\rm max}/\cos(\theta_w)$ and realistic $K_{\rm lid}$ values (i.e., $K_{\rm lid} \geq 2 \cdot 10^{-2}$ m^{-1} as in extremely oligotrophic waters), the exponential term could be neglected and Eq. (37) is approximated as:

$$P_n^w \approx \frac{T_s^2 \Delta\Omega_w^A \beta_\pi}{2K_{\rm lid}}. \tag{38}$$

In Fig. 13 the P_n^w values as a function of Chl-a in Case-1 waters are computed using both LiOC simulations and the analytical expression. Simulation runs are executed by tracing $5 \cdot 10^5$ rays for Chl-a<1, $8 \cdot 10^5$ rays for 1<Chl-a<10 and 10^6 for Chl-a>10 (with Chl-a in units of mg m^{-3}). The number of traced photons was determined to ensure a negligible effect of MC simulation noise. Each simulation is repeated three times, and the lines and the error bars of Fig. 13 represent the mean and the standard deviation of the three replicates. For the analytical expression, β_π (depending on Chl-a) was calculated as in Morel et al. [53]. A minimum and a

Optics EXPRESS

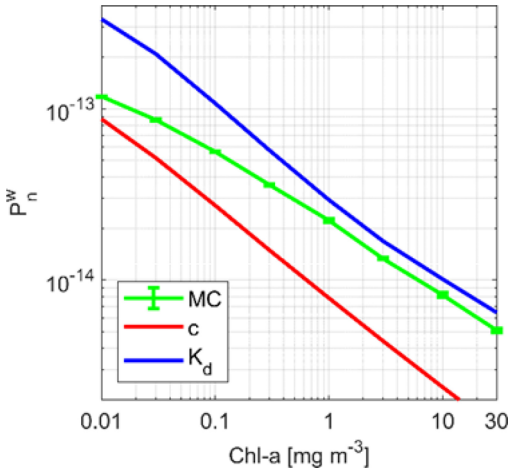

Fig. 13. Plot of P_n^w values as a function of Chl-*a* in the range 0.01 to 30 mg m^{-3} calculated with LiOC (green) and with the analytical expression using K_d (blue) and c (red) as K_{lid}.

maximum value of K_{lid} was considered for each Chl-*a* concentration, corresponding to K_d and c respectively.

Results show that when Chl-*a* increases from 0.01 to 30 mg m^{-3}, the P_n^w value reduces from about $1.2 \cdot 10^{-13}$ to about $5 \cdot 10^{-15}$. Admittedly, these comparison results could only prove that the MC model had failed (*i.e.*, if out of the expected range) but not its correctness under any applicative condition and, indeed, if the lidar equation could be used to validate the MC model fully, simulations would not be necessary. It is noted, however, that MC simulation results are not only within the expected extremes, but they also display the correct tendency as a function of the water turbidity, going from values approaching c at low Chl-*a* concentration to K_d at high concentrations. This comparison then supports the consistency of MC simulations under the assumptions adopted for the analytical expression.

4. Summary and concluding remarks

This work explored the feasibility of using the backscattered signal measured by ALADIN ADM-Aeolus at 355 nm to address OC applications. To this end, the LiOC radiative transfer tool has been developed to account for ALADIN instrumental characteristics, including the emitting/observing geometry, and focus the analysis on the signal propagation at the sea surface and in the water volume. The rationale for implementing this new simulation code is the lack of an alternative model with all the features required for the specific ALADIN analysis.

LiOC relies on a semianalytic 3D MC approach for radiative transfer simulations in the marine environment. The current version of the software includes the possibility of considering rays' transmission/reflection at a rough sea surface, absorption and multiple scattering in the seawater volumes, and reflection from the sea bottom. The inherent optical properties for ray tracing were currently defined based on pure seawater, Chlorophyll, and a generic absorber. Optical properties have been parametrized with algorithms/databases, which can be easily updated on demand.

The code modularity permits easy adaptation to other mission/lidar configurations and the inclusion of additional components/radiative processes. In particular:

- detailed emission/reception geometry and acquisition properties for any instrumental configuration can be easily simulated;

Optics EXPRESS

- based on the availability of bio-optical properties, data from other wavelengths can be considered;
- additional components (*e.g.*, sediments) can be included;
- simulation of non-elastic processes (e.g., Raman, fluorescence) from water components can be implemented, allowing, for example, the analysis of HSRL observations;
- fully polarized RT in the water can be taken into account besides that already implemented for the sea surface, providing the availability of scattering matrices for each considered component;
- interfaces with complementary tools to simulate the atmospheric path can be created, allowing for the top-of-atmosphere (TOA) signal simulation.

A simplified simulation scenario has been adopted in this study, particularly regarding the number of optical properties of each marine component and their spatial variability. Specifically, LiOC simulations were performed in a homogeneous water column because ALADIN measurements do not allow for resolving optical stratification in the ocean bin. Different backscattering sources that can contribute to ALADIN measurements have been analyzed to identify favorable conditions for OC applications. Results have shown that: 1) in oligotrophic waters (Chl-$a = 0.01$ mg m^{-3}), reflection from the sea floor contributes to less than 1% of the signal starting from a depth of 80 m, and 2) because of the slant illumination/collection geometry of ALADIN, sea-surface reflectance contribution to the ground-bin signal is negligible for surface wind intensity up to about 8 m s^{-1}.

It is reported that these results were then exploited to design screening flags for the processing of actual ALADIN observation and set a demonstrative framework for the inversion of ALADIN measurements into OC products (details are presented in a companion paper). The present work, instead, only focused on translating LiOC simulation results into a 3D LUT as a case study to demonstrate the possibility of estimating the total absorption at 355 nm as a function of the ALADIN measurements and Chl-a to be retrieved as ancillary information from an independent source. The novelty of this approach is to consider the CDOM parameterization only at a post-processing stage, which opens up opportunities for further development, such as investigating alternative spectral models of $a_{\mathrm{CDOM}}(\lambda)$. The capability to simulate ALADIN measurements was analyzed by showing that LiOC results are within upper and lower boundaries obtained through analytical models from the literature.

It is finally noted that this study was executed within the COLOR project of ESA. However, research objectives and results meet the interests of other space programs, such as including UV bands for OC remote sensing, as emphasized by the PACE mission of NASA. The study findings are also helpful in paving the way for the exploitation of data from future programs with similar characteristics, as ATLID-EarthCARE [69], and consolidating simulation tools for designing new spaceborne lidar missions dedicated to studying marine properties as the ASI-NASA CALIGOLA project.

Funding. European Space Agency (Contract No. 4000133933/21/I-BG.).

Acknowledgments. The authors acknowledge the helpful inputs and advices by Marie-Helene Rio of ESRIN-ESA during the COLOR project execution.

Disclosures. The authors declare no conflicts of interest.

Data availability. Data underlying the results presented in this paper are not publicly available at this time but may be obtained from the authors upon reasonable request.

References

1. M. Sammartino, S. Marullo, R. Santoleri, *et al.*, "Modelling the Vertical Distribution of Phytoplankton Biomass in the Mediterranean Sea from Satellite Data: A Neural Network Approach," Remote Sens. **10**(10), 1666 (2018).

Optics EXPRESS

2. D. D'Alimonte, F. Melin, G. Zibordi, *et al.*, "Use of the novelty detection technique to identify the range of applicability of empirical ocean color algorithms," IEEE Trans. Geosci. Remote Sensing **41**(12), 2833–2843 (2003).
3. M. Hieronymi, D. Müller, and R. Doerffer, "The OLCI Neural Network Swarm (ONNS): A Bio-Geo-Optical Algorithm for Open Ocean and Coastal Waters," Front. Mar. Sci. **4**, 140 (2017).
4. J. H. Churnside, "Review of profiling oceanographic lidar," Opt. Eng. **53**(5), 051405 (2014).
5. M. J. Behrenfeld, Y. Hu, R. T. O'Malley, *et al.*, "Annual boom–bust cycles of polar phytoplankton biomass revealed by space-based lidar," Nat. Geosci. **10**(2), 118–122 (2017).
6. C. A. Hostetler, M. J. Behrenfeld, Y. Hu, *et al.*, "Spaceborne Lidar in the Study of Marine Systems," Annu. Rev. Mar. Sci. **10**(1), 121–147 (2018).
7. C. Jamet, A. Ibrahim, Z. Ahmad, *et al.*, "Going Beyond Standard Ocean Color Observations: Lidar and Polarimetry," Front. Mar. Sci. **6**, 251 (2019).
8. D. Dionisi, V. E. Brando, G. Volpe, *et al.*, "Seasonal distributions of ocean particulate optical properties from spaceborne lidar measurements in Mediterranean and Black sea," Remote Sensing of Environment **247**, 111889 (2020).
9. X. Lu, Y. Hu, Y. Yang, *et al.*, "New Ocean Subsurface Optical Properties From Space Lidars: CALIOP/CALIPSO and ATLAS/ICESat-2," Earth and Space Science **8**(10), e2021EA001839 (2021).
10. X. Lu, Y. Hu, A. Omar, *et al.*, "Lidar attenuation coefficient in the global oceans: insights from ICESat-2 mission," Opt. Express **31**(18), 29107–29118 (2023).
11. X. Lu, Y. Hu, Y. Yang, *et al.*, "Antarctic spring ice-edge blooms observed from space by ICESat-2," Remote Sensing of Environment **245**, 1–8 (2020).
12. M. J. Behrenfeld, L. Lorenzoni, Y. Hu, *et al.*, "Satellite Lidar Measurements as a Critical New Global Ocean Climate Record," Remote Sens. **15**(23), 5567 (2023).
13. A. Stoffelen, J. Pailleux, E. Källén, *et al.*, "The atmospheric dynamics mission for global wind field measurement," Bull. Amer. Meteor. Soc. **86**(1), 73–88 (2005).
14. J. Hair, C. Hostetler, Y. Hu, *et al.*, "Combined Atmospheric and Ocean Profiling from an Airborne High Spectral Resolution Lidar," EPJ Web Conf. **119**, 22001 (2016).
15. J. A. Schulien, M. J. Behrenfeld, J. W. Hair, *et al.*, "Vertically- resolved phytoplankton carbon and net primary production from a high spectral resolution lidar," Opt. Express **25**(12), 13577 (2017).
16. D. Liu, Y. Zhou, W. Chen, *et al.*, "Phase function effects on the retrieval of oceanic high-spectral-resolution lidar," Opt. Express **27**(12), A654 (2019).
17. R. Liu, Q. Ling, Q. Zhang, *et al.*, "Detection of Chlorophyll a and CDOM Absorption Coefficient with a Dual-Wavelength Oceanic Lidar: Wavelength Optimization Method," Remote Sens. **12**(18), 3021 (2020).
18. D. A. Siegel, S. Maritorena, N. B. Nelson, *et al.*, "Global distribution and dynamics of colored dissolved and detrital organic materials," J. Geophys. Res. **107**(C12), 21 (2002).
19. D. A. Siegel, S. Maritorena, N. B. Nelson, *et al.*, "Colored dissolved organic matter and its influence on the satellite-based characterization of the ocean biosphere," Geophys. Res. Lett. **32**(20), 2005GL024310 (2005).
20. P. J. Werdell, L. I. W. McKinna, E. Boss, *et al.*, "An overview of approaches and challenges for retrieving marine inherent optical properties from ocean color remote sensing," Prog. Oceanogr. **160**, 186–212 (2018).
21. P. J. Werdell, M. J. Behrenfeld, P. S. Bontempi, *et al.*, "The Plankton, Aerosol, Cloud, Ocean Ecosystem Mission: Status, Science, Advances," Bull. Am. Meteorol. Soc. **100**(9), 1775–1794 (2019).
22. J. Oelker, S. N. Losa, A. Richter, *et al.*, "TROPOMI-Retrieved Underwater Light Attenuation in Three Spectral Regions in the Ultraviolet and Blue," Front. Mar. Sci. **9**, 787992 (2022).
23. D. Dionisi, S. Bucci, C. Cesarini, *et al.*, "Exploring the potential of Aeolus lidar mission for ocean color applications," [*isubmitted to Remote Sensing of the Environment*] (2024).
24. D. D'Alimonte, G. Zibordi, T. Kajiyama, *et al.*, "Monte Carlo code for high spatial resolution ocean color simulations," Appl. Opt. **49**(26), 4936–4950 (2010).
25. D. D'Alimonte and T. Kajiyama, "Effects of light polarization and waves slope statistics on the sea-surface reflectance," Opt. Express **24**(8), 7922–7942 (2016).
26. T. Kajiyama, D. D'Alimonte, and J. C. Cunha, "A high-performance computing framework for Monte Carlo ocean color simulations," Concurrency Computat.: Pract. Exper. **29**, e3860 (2017).
27. D. D'Alimonte, T. Kajiyama, G. Zibordi, *et al.*, "Sea-surface reflectance factor: replicability of computed values," Opt. Express **29**(16), 25217 (2021).
28. L. R. Poole, D. D. Venable, and J. W. Campbell, "Semianalytic Monte Carlo radiative transfer model for oceanographic lidar systems," Appl. Opt. **20**(20), 3653 (1981).
29. H. Abdallah, N. Baghdadi, J.-S. Bailly, *et al.*, "Wa-LiD: A New LiDAR Simulator for Waters," IEEE Geosci. Remote Sensing Lett. **9**(4), 744–748 (2012).
30. Q. Liu, D. Liu, J. Bai, *et al.*, "Relationship between the effective attenuation coefficient of spaceborne lidar signal and the IOPs of seawater," Opt. Express **26**(23), 30278 (2018).
31. Q. Liu, X. Cui, C. Jamet, *et al.*, "A Semianalytic Monte Carlo Simulator for Spaceborne Oceanic Lidar: Framework and Preliminary Results," Remote Sens. **12**(17), 2820 (2020).
32. P. Chen, D. Pan, Z. Mao, *et al.*, "Semi-Analytic Monte Carlo Model for Oceanographic Lidar Systems: Lookup Table Method Used for Randomly Choosing Scattering Angles," Appl. Sci. **9**(1), 48 (2019).

Optics EXPRESS

33. P. Chen, D. Pan, Z. Mao, *et al.*, "Semi-analytic Monte Carlo radiative transfer model of laser propagation in inhomogeneous sea water within subsurface plankton layer," Opt. Laser Technol. **111**, 1–5 (2019).
34. P. Chen, C. Jamet, Z. Mao, *et al.*, "OLE: A Novel Oceanic Lidar Emulator," IEEE Trans. Geosci. Remote Sensing **60**, 1–18 (2020).
35. S. Chen, P. Chen, L. Ding, *et al.*, "A New Semi-Analytical MC Model for Oceanic LIDAR Inelastic Signals," Remote Sens. **15**(3), 684 (2023).
36. Z. Zhang, P. Chen, and Z. Mao, "SOLS: An Open-Source Spaceborne Oceanic Lidar Simulator," Remote Sens. **14**(8), 1849 (2022).
37. P. Girolamo, A. Cosentino, F. Longo, *et al.*, "Introducing the Cloud Aerosol Lidar for Global Scale Observations of the Ocean-Land-Atmosphere System: CALIGOLA," in Proceedings of the 30th International Laser Radar Conference. Atmospheric Sciences. Springer, Cham pp. 625–630 (2022).
38. P. Di Girolamo, N. Franco, D. Dionisi, *et al.*, "The Cloud and Aerosol Lidar for Global Scale Observations of the Ocean-Land-Atmosphere System – CALIGOLA," Bulletin of the American Meteorological Society [in preparation] (2024).
39. C. Cox and W. Munk, "Measurement of the roughness of the sea surface from photographs of the sun's glitter," J. Opt. Soc. Am. **44**(11), 838–850 (1954).
40. C. Mobley, E. Boss, and C. Roesler, "Ocean Optics Web Book," https://www.oceanopticsbook.info/.
41. C. D. Mobley, "Estimation of the remote-sensing reflectance from above-surface measurements," Appl. Opt. **38**(36), 7442–7455 (1999).
42. J. I. Gordon, *Directional radiance (luminance) of the sea surface*, (Naval Ship Systems Command Department of the Navy, Washington, D. C. 20360, 1969).
43. M. L. Banner and D. H. Peregrine, "Wave Breaking in Deep Water," Annu. Rev. Fluid Mech. **25**(1), 373–397 (1993).
44. H. Czerski, I. M. Brooks, S. Gunn, *et al.*, "Ocean bubbles under high wind conditions – Part 1: Bubble distribution and development," Ocean Sci. **18**(3), 565–586 (2022).
45. X. Cui, Q. Liu, Q. Gu, *et al.*, "Influence of wind-roughed sea surface on detection performance of spaceborne oceanic lidar," Journal of Quantitative Spectroscopy and Radiative Transfer **297**, 108481 (2023).
46. A. A. Kokhanovsky, "Spectral reflectance of whitecaps," J. Geophys. Res. **109**(C5), 2003JC002177 (2004).
47. R. Röttgers, R. Doerffer, D. McKee, *et al.*, *The Water Optical Properties Processor (WOPP) Pure Water Spectral Absorption, Scattering, and Real Part of Refractive Index Mode*l (ESA/ESRIN, 2016), pp. 1–20.
48. J. D. Mason, M. T. Cone, and E. S. Fry, "Ultraviolet (250–550 nm) absorption spectrum of pure water," Appl. Opt. **55**(1), 7163–7172 (2016).
49. A. Bricaud, A. Morel, and L. Prieur, "Absorption by dissolved organic matter of the sea (yellow substance) in the UV and visible domains1," Limnol. Oceanogr. **26**(1), 43–53 (1981).
50. J. Pitarch, "Biases in ocean color over a Secchi disk," Opt. Express **25**(24), A1124 (2017).
51. E. Terzić, A. Miró, E. Organelli, *et al.*, "Radiative Transfer Modeling With Biogeochemical-Argo Float Data in the Mediterranean Sea," JGR Oceans **126**(10), e2021JC017690 (2021).
52. H. Loisel and A. Morel, "Light scattering and chlorophyll concentration in case 1 waters: A reexamination," Limnol. Oceanogr. **43**(5), 847–858 (1998).
53. A. Morel, D. Antoine, and B. Gentili, "Bidirectional reflectance of oceanic waters: accounting for Raman emission and varying particle scattering phase function," Appl. Opt. **41**(30), 6289 (2002).
54. G. R. Fournier, "Backscatter corrected Fournier-Forand phase function for remote sensing and underwater imaging performance evaluation," in Current Research on Remote Sensing, Laser Probing, and Imagery in Natural Waters, I. M. Levin, G. D. Gilbert, V. I. Haltrin, and C. C. Trees, eds. (2007), pp. 66150N-66150N–7.
55. G. R. Fournier and J. L. Forand, "Analytic Phase Function for Ocean Water," in *Ocean Optics XII* (SPIE, 1994), pp. 194–201.
56. M. I. Mishchenko and L. D. Travis, "Capabilities and limitations of a current FORTRAN implementation of the T-matrix method for randomly oriented, rotationally symmetric scatterers," J. Quant. Spectrosc. Radiat. Transfer **60**(3), 309–324 (1998).
57. P. C. Waterman, "Matrix formulation of electromagnetic scattering," Proc. IEEE **53**(8), 805–812 (1965).
58. A. Morel, Y. Huot, B. Gentili, *et al.*, "Examining the consistency of products derived from various ocean color sensors in open ocean (Case 1) waters in the perspective of a multi-sensor approach," Remote Sensing of Environment **111**(1), 69–88 (2007).
59. S. Sathyendranath, T. Platt, C. M. Caverhill, *et al.*, "Remote sensing of oceanic primary production: computations using a spectral model," Deep-Sea Res., Part A **36**(3), 431–453 (1989).
60. H. R. Gordon, "Interpretation of airborne oceanic lidar: effects of multiple scattering," Appl. Opt. **21**(16), 2996–3001 (1982).
61. S. Maritorena, A. Morel, and B. Gentili, "Diffuse reflectance of oceanic shallow waters: Influence of water depth and bottom albedo," Limnol. Oceanogr. **39**(7), 1689–1703 (1994).
62. C. D. Mobley, *Light and Water. Radiative Transfer in Natural Waters* (Academic, San Diego, U.S., 1994).
63. T. Elfouhaily, B. Chapron, K. Katsaros, *et al.*, "A unified directional spectrum for long and short wind-driven waves," J. Geophys. Res. Oc. **102**(A1), 1 (1997).
64. O. Reitebuch, D. Huber, and I. Nikolaus, "Algorithm Theoretical Basis Document ATBD: ADM-Aeolus Level 1B Products," *Tech. rep.* (2018).

Optics EXPRESS

65. WGS84, "Department of Defense World Geodetic System 1984," https://web.archive.org/web/20170704192233/http://earth-info.nga.mil/GandG/publications/tr8350.2/tr8350_2.html.
66. S. E. Brumer, C. J. Zappa, I. M. Brooks, *et al.*, "Whitecap Coverage Dependence on Wind and Wave Statistics as Observed during SO GasEx and HiWinGS," Journal of Physical Oceanography **47**(9), 2211–2235 (2017).
67. C. L. Archer, "Evaluation of global wind power," J. Geophys. Res. **110**(D12), D12110 (2005).
68. D. M. Phillips and B. W. Koerber, "A Theoretical Study of an Airborne Laser Technique for determining Sea Water Turbidity," Aust. J. Phys. **37**(1), 75–90 (1984).
69. A. J. Illingworth, H. W. Barker, A. Beljaars, *et al.*, "The EarthCARE Satellite: The Next Step Forward in Global Measurements of Clouds, Aerosols, Precipitation, and Radiation," Bull. Am. Meteorol. Soc. **96**(8), 1311–1332 (2015).